Journal of Geophysical Research: Atmospheres

RESEARCH ARTICLE
10.1029/2018JD029161

Key Points:
- Enhancement of precipitation processes is found in radar reflectivity data above the melting level over complex terrain
- Enhancement aloft is especially pronounced during periods of high vapor transport, onshore flow, and neutral low-level static stability
- Satellite-borne radar detects this enhancement so that reliable estimates of precipitation over remote mountain regions are possible

Correspondence to:
L. A. McMurdie,
lynnm@uw.edu

Citation:
McMurdie, L. A., Rowe, A. K., Houze, R. A., Jr, Brodzik, S. R., Zagrodnik, J. P., & Schuldt, T. M. (2018). Terrain-enhanced precipitation processes above the melting layer: Results from OLYMPEX. *Journal of Geophysical Research: Atmospheres*, *123*. https://doi.org/10.1029/2018JD029161

Received 11 JUN 2018
Accepted 12 OCT 2018
Accepted article online 18 OCT 2018

Terrain-Enhanced Precipitation Processes Above the Melting Layer: Results From OLYMPEX

L. A. McMurdie[1], A. K. Rowe[1], R. A. Houze Jr[1,2], S. R. Brodzik[1], J. P. Zagrodnik[1], and T. M. Schuldt[1,3]

[1]Department of Atmospheric Sciences, University of Washington, Seattle, WA, USA, [2]Pacific Northwest National Laboratory, Richland, WA, [3]The Narwhal Group, Bellevue, WA

Abstract Enhancement of precipitation processes aloft over complex terrain is documented using reflectivity data from an S-band scanning radar (NPOL) that was deployed on the west coast of Washington State during the Olympic Mountains Experiment (OLYMPEX). From November 2015 through mid-January 2016, NPOL obtained high-resolution data within sectors over the ocean and over the windward slopes of the Olympic Mountains. Contoured Frequency by Altitude Diagrams of radar reflectivity highlight a higher frequency of occurrence of larger reflectivities for all heights between 2 and 8 km over land compared to ocean, with the largest difference in the 4- to 6-km range indicating a robust signature of enhancement aloft over the windward slopes. This enhancement pattern is found to some degree under all environmental conditions considered but is especially pronounced during periods of high vapor transport, high melting level height, southwest low-level winds, and neutral stability. These conditions are generally associated with warm sectors of midlatitude cyclones and atmospheric rivers. Past studies have postulated that a secondary enhancement in reflectivity aloft was an intrinsic part of atmospheric river type systems. However, these results show that further significant enhancement of this signature occurs as deep moist-neutral, high water vapor content flow is lifted when it encounters a mountain range. Reflectivity data from the dual-precipitation radar aboard the Global Precipitation Measurement satellite also documents this reflectivity increase aloft over the Olympic Mountains compared to the adjacent ocean, showing the potential for Global Precipitation Measurement to provide reliable estimates of precipitation structure over remote mountainous regions.

Plain Language Summary When frontal cyclones pass over a mountain range, modification of flow often results in precipitation enhancement on the windward slopes. Most studies of this phenomenon rely on the precipitation patterns deduced from surface networks of rain gauges or through numerical modeling. Little attention has been given to orographic modification of the precipitation processes occurring in the middle and upper layers of clouds. This paper uses high-resolution vertical cross sections of radar reflectivity data taken during the Olympic Mountains Experiment. Measurements made over the ocean are compared to those over the windward slopes of the Olympic Mountains and a clear signature of enhancement aloft over the windward slopes is found at all heights from 2 to 8 km strongest between 4 and 6 km. This enhancement of reflectivity aloft is especially pronounced under environmental conditions of large water vapor transport, high melting level, strong onshore-directed low-level winds and neutral stability. Those environmental conditions are commonly found in warm sectors of midlatitude cyclones and in atmospheric river-type events. This same signature of higher reflectivity aloft over windward slopes is found from satellite-derived radar reflectivity measurements implying that satellites have the potential to provide reliable estimates of precipitation structure over remote mountainous regions.

1. Introduction

Precipitation resulting from moist air flowing over and around mountains contributes strongly to the global precipitation distribution. The modification of the three-dimensional flow field by complex terrain affects precipitation-forming processes throughout the vertical depth of the moist flow. In the literature, modification of precipitation by mountains is usually described by surface precipitation patterns, surface rain gauge and/or SNOw TELemetry (SNOTEL) networks, or through modeling (e.g., Daly et al., 1994; Lewis et al., 2017; Minder et al., 2008; Neiman et al., 2002; Zagrodnik et al., 2018). However, little attention has been given to the orographic modification of the precipitation processes occurring in the middle and upper layers of clouds. In the formulation of their linear theory of orographic precipitation, Smith and Barstad (2004) assumed that precipitation particle fallout was controlled by the vertical air motion resulting from flow over a mountain acting on a saturated column but did not specify how microphysical processes aloft were modified by the orographically affected airflow.

Environmental characteristics of the upstream flow that have a strong influence on the distribution and intensity of precipitation in regions of complex terrain include wind direction, wind speed, stability, melting level height, and water vapor flux. Modeling studies have shown that the direction of the upstream low-level flow determines the location of maximum precipitation on the windward slopes, especially in the case of a three-dimensional barrier (Minder et al., 2008; Nuss & Miller, 2001; Picard & Mass, 2017). Both the strength of the incoming flow and the static stability determine whether the incoming low-level flow has enough energy to surmount a given mountain barrier or is blocked and deflected, and the distribution and intensity of orographic precipitation has been shown to vary according to whether the flow is blocked or unblocked (Garvert et al., 2007; Houze et al., 2001; James & Houze, 2005; Neiman et al., 2013; Steenburgh, 2003). The intensity of the incoming moisture flux is a strong control on the distribution and intensity of precipitation in complex terrain (Neiman et al., 2011; Purnell & Kirshbaum, 2018; Steenburgh, 2003; Zagrodnik et al., 2018). The temperature profile is especially important from a microphysical viewpoint; when the melting level is high, warm-rain processes of collision and coalescence act over a deeper layer and contribute to the subsequent distribution of precipitation. Zagrodnik et al. (2018) showed that when the melting layer is high over the Olympic Mountains, warm-rain processes contribute to raindrop size distributions dominated by large quantities of small-to-medium sized drops on the lower-elevation windward slopes. The overall message of these prior studies is to emphasize the importance of environmental controls on the modification of precipitation in complex terrain, yet nearly all of these works have defined this enhancement in terms of the resulting intensity and distribution of precipitation at the ground and did not consider how these environmental characteristics relate to precipitation processes aloft.

To document the extent of modification of the precipitation processes at middle and upper levels, we use three-dimensional radar observations with fine resolution in the vertical. Operational radar data (e.g., the Weather Surveillance Radar 1988 Doppler, or WSR-88D network) are routinely collected in plan position indicator (PPI) mode, where radar reflectivity is measured as the antenna rotates azimuthally at a discrete set of elevation angles. This scanning strategy provides important spatial coverage at high horizontal resolution but limits detailed studies on microphysical processes due to relatively coarser vertical resolution. Range-height indicator (RHI) scans, where vertical scans are made at specific azimuth angles, provide detailed vertical information. During the Olympic Mountains Experiment (OLYMPEX, Houze et al., 2017), an S-band scanning radar located on the coast of Washington State operated in RHI mode (i.e., changing elevation angles at a constant azimuthal angle), with RHI sectors focused both upstream over the Pacific Ocean and downstream over the southwestern slopes as midlatitude wintertime storms approached the Olympic Mountains.

Previous studies have examined processes contributing to orographic enhancement of precipitation on the west coast of the United States with S-band profilers. These vertically pointing radars showed enhancements of reflectivity aloft. Kingsmill et al. (2006) noted a secondary reflectivity enhancement aloft in storms passing over complex terrain in coastal California, but attributed this feature to the large-scale dynamic, thermodynamic, and microphysical structure of the storm itself and not as a result of enhancement due to lifting over mountains. Medina et al. (2007) arrived at a different conclusion in a study of occluded frontal systems passing over the Oregon Cascades. They also found an enhancement of reflectivity at about 1–2.5 km above the bright band when the middle sector of the storm passed over the windward slope of the Cascades. They suggested that this feature results from or is enhanced by flow modification by the underlying terrain. In their study, the middle sector of the storm was characterized by vertically continuous radar echo extending from the mountainside up to a height of approximately 5–6 km that lasted for several hours. While both studies noted the presence of the secondary reflectivity maximum aloft, they were limited by case studies and by the high vertical resolution radar data existing only in an Eulerian vertical profile that lacked horizontal continuity extending upstream and over the mountains.

The goal of this paper is to determine if an upper-level enhancement in radar reflectivity was observed over the terrain during OLYMPEX and, if present, document its horizontal and vertical variability and its

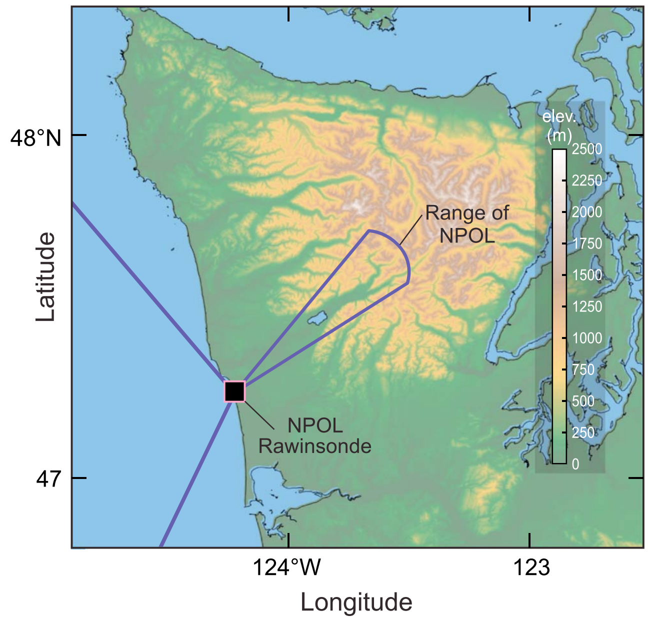

Figure 1. Map of the Olympic Peninsula with terrain elevation in meters (shaded). The black square is the location of the NASA S-band dual-polarization Doppler radar (NPOL) and where soundings were launched. The ocean and land NPOL RHI sectors are indicated with dark blue lines.

relationship to environmental conditions. In section 3, we compare radar reflectivity statistics from continuous RHI scans (with fine vertical resolution) over the ocean to those over the windward slopes of the Olympic Mountains during OLYMPEX and explore how the differences between radar reflectivity over the ocean and land vary due to environmental conditions in sections 4 and 5. The ability of satellite radar reflectivity (which also has fine vertical resolution) to detect the signature of enhancement over complex terrain is presented in section 6 followed by discussion and conclusions in section 7.

2. Data and Methods

2.1. OLYMPEX Data

There were two intensive observing periods (IOPs) during OLYMPEX, occurring 12 November to 19 December 2015 and 4–15 January 2016 (see Petersen et al., 2018, for all available OLYMPEX data). During the IOPs, a NASA dual-polarization Doppler S-band radar (NPOL) operated nearly continuously from the southwestern coast of the Olympic Peninsula (47.277°N, 124.211°W; Figure 1). The radar scanning strategy consisted primarily of RHI scans, with an oceanic sector of 40 RHIs covering 210–326° in azimuth and a narrower sector centered on the Quinault River Valley with 16 RHIs over azimuths of 30° to 60°. The RHIs extended up to a 45° elevation angle, providing high vertical resolution cross sections out to 150-km range with a gate spacing of 125 m. With interspersed low-elevation PPI scans and vertically pointing scans, the entire scan sequence repeated every 20 min throughout the IOPs. Version 2 of the NPOL data set (Wolff et al., 2017) is used in this study. The radar reflectivity factor (Z_H) obtained by NPOL was calibrated via self-consistency methods and through comparison with disdrometer data. The calibration was consistent throughout NPOL operations with reflectivity reliable within 1 dB. Additional details on quality control of NPOL data can be found in Wolff et al. (2015) and Pippitt et al. (2015).

During the first IOP, soundings were launched via the Colorado State University Sounding Unit in coordination with the timing of storms of interest and aircraft operations as frequent as every 3 hr from the NPOL site. These rawinsondes were quality controlled following Ciesielski et al. (2012), provided as a research-quality data set with quality control flags, and are available from Rutledge et al. (2018). Routine National Weather Service Quillayute soundings were launched further north from NPOL at 0000 and 1200 UTC every day (also available in Rutledge et al., 2018). For the purpose of this study, both sets of soundings were used to verify the representativeness of reanalysis data for this region.

2.2. NARR Data Set

The synoptic data used to describe the thermodynamic and dynamic properties of moist flow impinging on the Olympic Mountains are from the North American Regional Reanalysis (NARR; Mesinger et al., 2006). The NARR data set (NOAA/OAR/ESRL PSD, 2004) is available every 3 hr at 32-km horizontal and 25-hPa vertical resolutions throughout the entire duration of NPOL operations. Following Zagrodnik et al. (2018), the 925-hPa wind magnitude and direction provided the low-level flow context. The NARR derived 3-hr horizontal water vapor flux accumulation parameter was converted to instantaneous integrated vapor transport (IVT; kg m^{-1} s^{-1}) to describe the moisture flux into the region. Similar to Medina and Houze (2015), a measure of low-level static stability over the 950- to 850-hPa layer is given via the moist Brunt Väisälä frequency (N_m^2) following Durran and Klemp (1982). Melting level height is determined by linearly interpolating the heights between the highest level with a temperature above 0 °C and the next level (at 25-hPa vertical resolution) directly above. These parameters were computed for the 0.3° grid box centered closest to the location of NPOL (where soundings were launched) and linearly interpolated in time by seconds to match the NPOL data (available every 20 min). Histograms of melting level heights calculated with the NARR reanalysis data and NPOL soundings shown in Figure 2 highlight a reasonable comparison with mean heights within about 10 m of each other, mean absolute difference of 143 m, and a high correlation coefficient of 0.94. The other

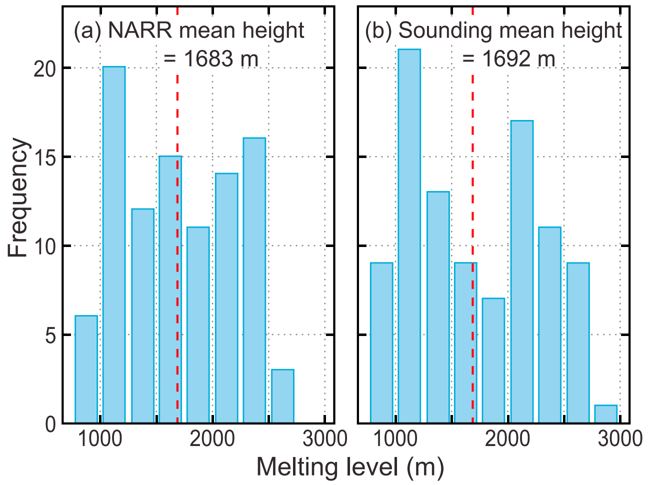

Figure 2. Comparison of the (a) NARR and (b) NPOL sounding melting level height histograms. The NARR soundings were computed for the 0.3° grid box centered closest to the location of NPOL and linearly interpolated in time by seconds to match the NPOL sounding launch time. Vertical red dash lines indicate the mean melting level height for each data source.

parameters (IVT, N_m^2 and wind direction) were also compared (not shown). The mean NARR IVT was lower than the mean NPOL soundings IVT by 98 kg m^{-1} s^{-1} but was highly correlated at 0.95. The mean wind directions from both data sets were nearly identical and also highly correlated. The stability parameter, N_m^2, had a lower correlation coefficient (0.78) largely due to the differences in vertical resolution of the NARR compared to the detailed soundings. There were rare occasions when NARR and the observed NPOL soundings had large differences in these parameters that were largely due to sharp frontal passages that the NARR data could not resolve accurately. Nevertheless, with the high correlation coefficients the NARR parameters are used to evaluate the broad environmental context of the NPOL radar observations.

2.3. CFADS

Contoured Frequency by Altitude Diagrams (CFADs; Yuter & Houze, 1995) of NPOL reflectivity data were created to statistically display radar echo from all NPOL RHIs over the ocean (upstream) and all RHIs from the land sector over the windward slopes of the Olympic Mountains. NPOL RHI data were interpolated to a Cartesian grid with 0.5-km vertical resolution and 1.0-km horizontal resolution, then, for each 0.5-km height bin between 2 and 8 km, the frequency of occurrence of reflectivity from 0 to 45 dBZ, binned at 1-dBZ intervals, was computed to create the CFADs. We focused on 2 km and above in height to reduce contamination by ground clutter from the mountains and to avoid beam blockage. A maximum of 45 dBZ was used to eliminate exceptionally intense echo associated with remaining ground clutter over the mountains. The 8-km maximum height threshold reflects the typical echo-top height during periods of widespread stratiform precipitation, which was commonly observed during OLYMPEX (Zagrodnik et al., 2018). Frequencies of occurrence were normalized by level, meaning each frequency was normalized by the maximum frequency over all reflectivity bins at each height level, providing values ranging from 0 to 1 at each height.

2.4. Dual Precipitation Radar Data

A major goal of the OLYMPEX field campaign was to provide physical validation of the precipitation algorithms for the Global Precipitation Measurement (GPM) core observatory and consortium of satellites (Houze et al., 2017; Skofronick-Jackson et al., 2017). GPM was designed to measure rain rates from 0.2 to 110.0 mm/hr under a wide range of meteorological conditions. One of the instruments on GPM is the Dual Precipitation Radar (DPR), a Ka-/Ku-band radar that measures the three-dimensional structures of precipitating systems. In this study we use both frequency bands to compare to the results obtained from the NPOL S-band radar described above. The GPM DPR Ka Precipitation Profile 2A V05 (Iguchi & Meneghini, 2016a) and Ku Precipitation Profile 2A V05 (Iguchi & Meneghini, 2016b) was used in this study. Both data sets are vertical profiles of attenuation-corrected reflectivity factor with a 5 km × 5 km horizontal resolution and 125-to 250-m vertical resolution. The nominal sensitivities of these radars are 18 dBZ for the Ku band and 12 dBZ for the Ka high sensitivity scan, but Toyoshima et al. (2015) report that the Ku radar sensitivity is better at roughly 14 dBZ.

The DPR data were further processed in the same manner as described in Houze et al. (2007, 2015). The GPM DPR Ka and Ku 2A V05 data recorded along the radar beams were reprocessed by geolocating the data that were recorded along the slant range of the radar beam and interpolated onto a Cartesian grid. This three-dimensional geolocated and interpolated radar reflectivity data set are available at gpm.atmos.washington.edu. In this study, CFADs constructed from this 3-D data set from the Ku and Ka bands of DPR were calculated from all the GPM overpasses during the cold season (November through March) over the Olympic Peninsula between launch (28 February 2014) and March 2017. The region defined as land is the box from 46.5 to 48.6°N and 124.3 to 122.6°W, which encompasses the entire Olympic Peninsula, and ocean is the box from 46.5 to 48.6°N and 126.4 to 124.7°W, which is a box of the same width over the adjacent Pacific Ocean.

10.1029/2018JD029161

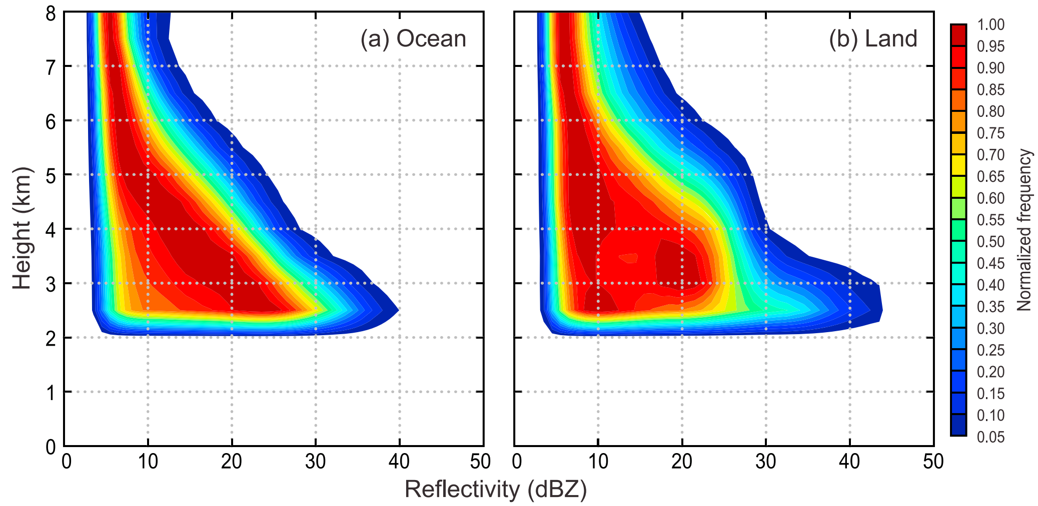

Figure 3. Contoured Frequency by Altitude Diagrams (CFADs) calculated from all NPOL RHI sectors over the (a) ocean and (b) land during the entire period of NPOL operations. The CFADs are normalized by level where each frequency is divided by the maximum frequency at each height level and shaded from 0 (blue) to 1 (red). Data are shown for heights above 2 km and reflectivity values between 5 and 45 dBZ.

3. Land Versus Ocean CFADs

Normalized reflectivity CFADs (as described in section 2.3) for all ocean (a) and land (b) NPOL RHIs are shown in Figure 3. The most frequent reflectivity at each level (modal value) generally slopes toward lower reflectivities with increasing height in both CFADs. This narrow diagonalization is especially pronounced over the ocean, where a sharp decrease in the most frequent reflectivity bin occurs with height, indicating a dominance of mature stratiform echo (e.g., Yuter & Houze, 1995). In both CFADs, the highest reflectivities (around 40 dBZ) occur between 2 and 3 km; a typical height range for the melting level during the relatively warm, stratiform events often observed in OLYMPEX (e.g., Zagrodnik et al., 2018). A shift toward higher frequency of reflectivities greater than 35 dBZ in this melting layer and a noticeable bulge aloft in the frequency of reflectivity greater than 20 dBZ between 4 and 6 km are observed over the windward slopes, suggesting an overall enhancement in reflectivity compared to upstream over the ocean.

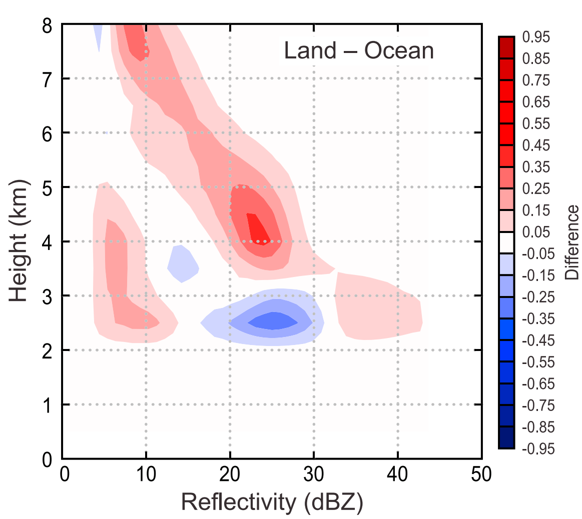

Figure 4. The difference between the normalized CFAD for the land sector and the normalized CFAD for the ocean sector. Red (blue) shades indicate relatively higher (lower) frequencies of reflectivity at that height bin over land compared to over ocean.

To further emphasize these differences, the normalized frequencies of reflectivity from NPOL RHIs over the ocean are subtracted from those over land and shown in Figure 4. The positive (red) values indicate greater frequencies of a given reflectivity over land, including the windward slopes of the mountains. Enhancement over land is observed when higher frequencies shift to the right toward higher reflectivities. In Figure 4 this enhancement is apparent at all levels between 2 and 8 km with the largest positive values between 4 and 5 km. The higher frequency of reflectivities greater than 35 dBZ and lower frequency of reflectivities less than 30 dBZ between 2 and 3 km over the land suggests a shift toward an increase in radar brightband intensity over the windward slopes as well. CFADs constructed relative to the brightband height (i.e., the 0 °C isotherm level) showed the same features described above, with a secondary enhancement layer at 2.5 km above the brightband and a shift toward an increase in radar brightband intensity over the windward slopes (not shown).

These figures highlight that in addition to the overall enhancement in precipitation totals at the ground over the windward slopes of the Olympic Mountains seen in the climatology (Houze et al., 2017; Minder et al., 2008; Zagrodnik et al., 2018), these precipitation-producing systems are also characterized by enhancement aloft throughout the depth of the precipitating system. The peak of this reflectivity enhancement aloft over land occurs around 4–5 km in height, or roughly 1.5 km or more above the melting layer during OLYMPEX, similar to the height of the secondary reflectivity maximum reported by Medina et al. (2007). The increase of radar reflectivity aloft that occurs between the upstream ocean area and the mountain slopes is a quantitative indication of the enhancement of the hydrometeor concentration aloft produced by the ascent of air over the terrain. Combined with knowledge of the increase of precipitation on the ground over the windward slopes (Zagrodnik et al., 2018), these radar data statistics provide a three-dimensional view of the orographic enhancement of the precipitation production when frontal systems move over a west coastal mountain range.

4. Variation of Enhancement With Environmental Conditions

The pattern of enhancement in the reflectivity difference CFAD (Figure 4) was based on RHI scans obtained in precipitating conditions regardless of meteorological conditions. In this section, we examine whether there are particular environment conditions under which these reflectivity differences are most pronounced.

As described above in section 2.2, four environmental parameters on the coast at the NPOL location (IVT, 925-hPa wind direction, melting level, and moist static stability) were determined from the NARR data. Each parameter is grouped into three categories that roughly correspond to different sectors of midlatitude cyclones (prefrontal, warm sector, and postfrontal). These sectors are inspired by the early study of Nagle and Serebreny (1962), defined by Medina et al. (2007), and applied to OLYMPEX by Houze et al. (2017) and Zagrodnik et al. (2018).

These qualitative storm-sector categories correspond approximately to values of the environmental parameters examined here.

1. The mean IVT when precipitation was observed during OLYMPEX was 340 kg m^{-1} s^{-1} (Zagrodnik et al., 2018). Based on this value, and the commonly used intensity threshold for atmospheric rivers of 250 kg m^{-1} s^{-1} (Moore et al., 2012; Rutz et al., 2014), storm sector categories are defined as less than 250 kg m^{-1} s^{-1} (~postfrontal), between 250 and 450 kg m^{-1} s^{-1} (~prefrontal), and greater than 450 kg m^{-1} s^{-1} (~warm sector).
2. The 925-hPa wind direction categories are 90–180° (~prefrontal), 180–270° (~warm sector), and 270–90° (~postfrontal).
3. The mean melting level height during periods of stratiform precipitation during OLYMPEX was roughly 1,800 m (Zagrodnik et al., 2018), and the mean melting level height is 1,400 m during moist onshore flow based on a climatology of soundings taken during the cold season on the coast of the Olympic Peninsula at Quillayute (Minder et al., 2008). Therefore, the melting level categories considered in this study are $<$1,200 m (~postfrontal), 1,200–1,800 m (~prefrontal), and $>$1,800 m (mostly warm sector and some prefrontal conditions). A melting level below 1,200 m results in widespread snow in the interior of the Olympic Mountains, 1,200–1,800 m restricts snow to the higher ridges, and 1,800 m results in widespread rain on all but the highest peaks.
4. The moist static stability parameter categories (following Zagrodnik et al., 2018) are moist unstable, $< -0.25 \times 10^{-4}$ s^{-2} (~postfrontal), moist neutral, between -0.25×10^{-4} s^{-2} and 0.25×10^{-4} s^{-2} (~warm sector), and moist stable, $>0.25 \times 10^{-4}$ s^{-2} (~prefrontal).

Difference reflectivity CFADs are presented for each of the aforementioned categories in Figure 5, including the relative percentage of time in which each subcategory occurred at NPOL during OLYMPEX. Each plot is arranged such that each vertical column corresponds roughly to different storm sectors, with the left column representing conditions often associated with the postfrontal sector (e.g., an unstable atmosphere with low melting level and IVT and winds from the west or northwest), the middle column representing conditions often associated with the warm sector (high IVT, southwesterly winds, high melting level, and neutral stability), and the right column representing conditions characteristic of the prefrontal regime (moderate IVT, southeast winds, moderate melting level height, and stable conditions). Note, however, that these specific thresholds of each environmental parameter do not all always coincide with the same storm sector. For example, only four time periods met all four prefrontal conditions, including one period sampling a decaying storm system and one period that had precipitation mostly over the ocean (it had not reached the land yet). More generally, a particular storm may be warmer (or colder) than average such that the

10.1029/2018JD029161

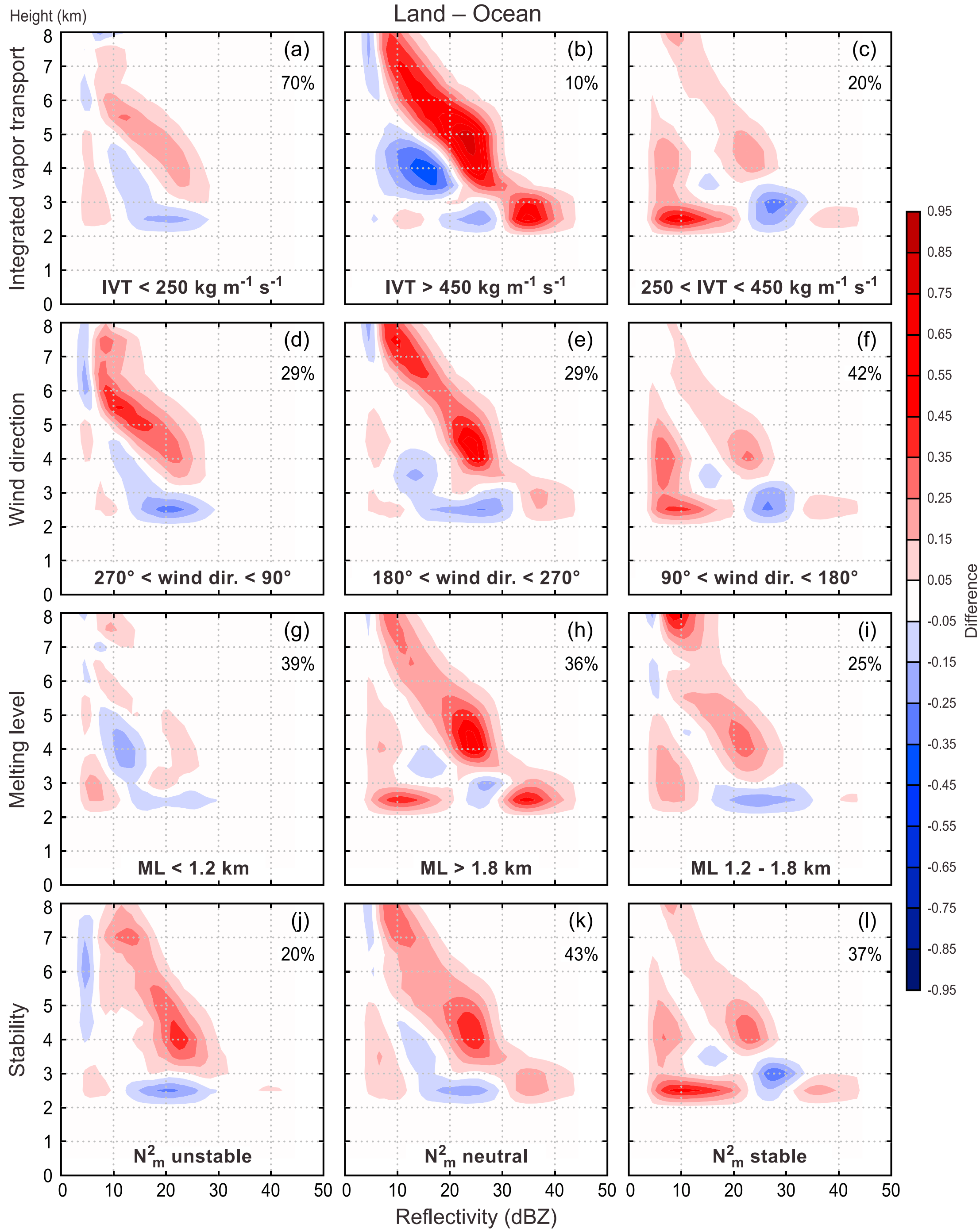

Figure 5. Difference CFADs of land minus ocean for different environmental conditions calculated from the NARR data closest to NPOL's location. Red (blue) shades indicate relatively higher (lower) frequencies of reflectivity at that height bin over land compared to over ocean. (top row) Integrated vapor transport (IVT) of (a) less than 250 kg m^{-1} s^{-1}, (b) greater than 450 kg m^{-1} s^{-1}, and (c) greater than 250 kg m^{-1} $s^{-1}$and less than 450 kg m^{-1} s^{-1}. (second row) Wind direction at 925 hPa with values (d) greater than 270° and less than 90°, (e) greater than 180° and less than 270°, and (f) greater than 90° and less than 180°. (third row) Melting level height of (g) less than 1.2 km, (h) greater than 1.8 km, and (i) greater than 1.2 km and less than 1.8 km. (bottom row) Moist static stability characterized as (j) unstable, (k) neutral, and (l) stable. The percentage of time that each environmental condition was observed during NPOL operations is shown in the upper right of each panel.

prefrontal environment as determined by careful synoptic frontal analysis may have a melting level height greater than 1.8 km (or a melting level height less than 1.2 km). The strength of our environmental parameter approach is that it does not require a synoptic frontal analysis for each event and only depends on the values of the environmental parameters.

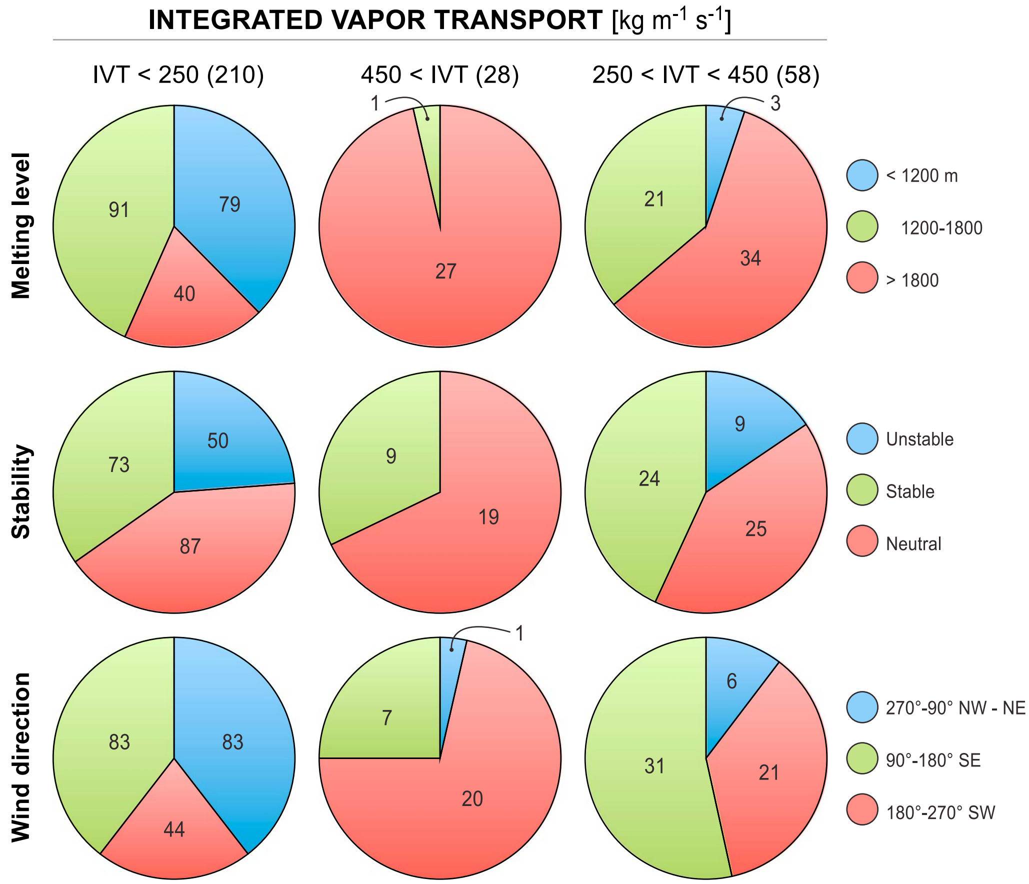

Figure 6. Relative percentage of melting level (top row), stability (middle row), and wind direction (bottom row) that occurred concurrently with integrated vapor transport (IVT) values of less than 250 kg m^{-1} s^{-1} (left column), greater than 450 kg m^{-1} s^{-1} (middle column), and between 250 and 450 kg m^{-1} s^{-1} (right column). The total number of events for each IVT category is given in parentheses at the top of each column, and the number of events for each of the other environmental parameters is given within each individual category.

At a glance, the upper-level reflectivity enhancement over land described in the previous section occurs, to some degree, in all categories of the four environmental parameters examined. Focusing on the three categories for IVT (Figures 5a–5c, first row), there is a shift to higher frequency of occurrence of higher reflectivity values at all height levels over land during periods when IVT was >450 kg m^{-1} s^{-1}, which occurred only 10% of the time. The differences are especially large between 2–3 km, which is associated with a stronger bright band, and between 4–5 km. High IVT greater than 450 kg m^{-1} s^{-1} is usually accompanied by a melting level greater than 1,800 m, southwest winds at 925 hPa, and moist neutral stability (Figure 6). These conditions are typical during atmospheric river events along the west coast (Neiman et al., 2002; Ralph et al., 2004; Zagrodnik et al., 2018). In contrast, when IVT is <250 kg m^{-1} s^{-1}, the enhancement is weaker but still present above 3 km indicating that orographic influences on the precipitation processes aloft occur under all IVT conditions to some degree. Note that unlike high IVT being mostly associated with high melting level, neutral stability, and southwesterly winds, the low IVT periods are more evenly distributed between all categories of the other environmental parameters (Figure 6). Even though we have labeled IVT < 250 kg m^{-1} s^{-1} as typical for postfrontal conditions, low IVT values can occur in a wide variety of synoptic conditions such as neutral stability, moderate melting level, or all wind directions. IVT category limits shifted ±50 kg m^{-1} s^{-1} (e.g., IVT < 200 kg m^{-1} s^{-1}, between 200 and 400 kg m^{-1} s^{-1}, and greater than 400 kg m^{-1} s^{-1}) were tested and the results were nearly identical to those described above.

Similar to IVT, all categories of 925-hPa wind direction exhibit a shift to a greater frequency of occurrence of high reflectivity values at all height levels over the land, but the enhancement at all heights over land is especially pronounced during periods with southwest winds (Figures 5d–5f, second row). This

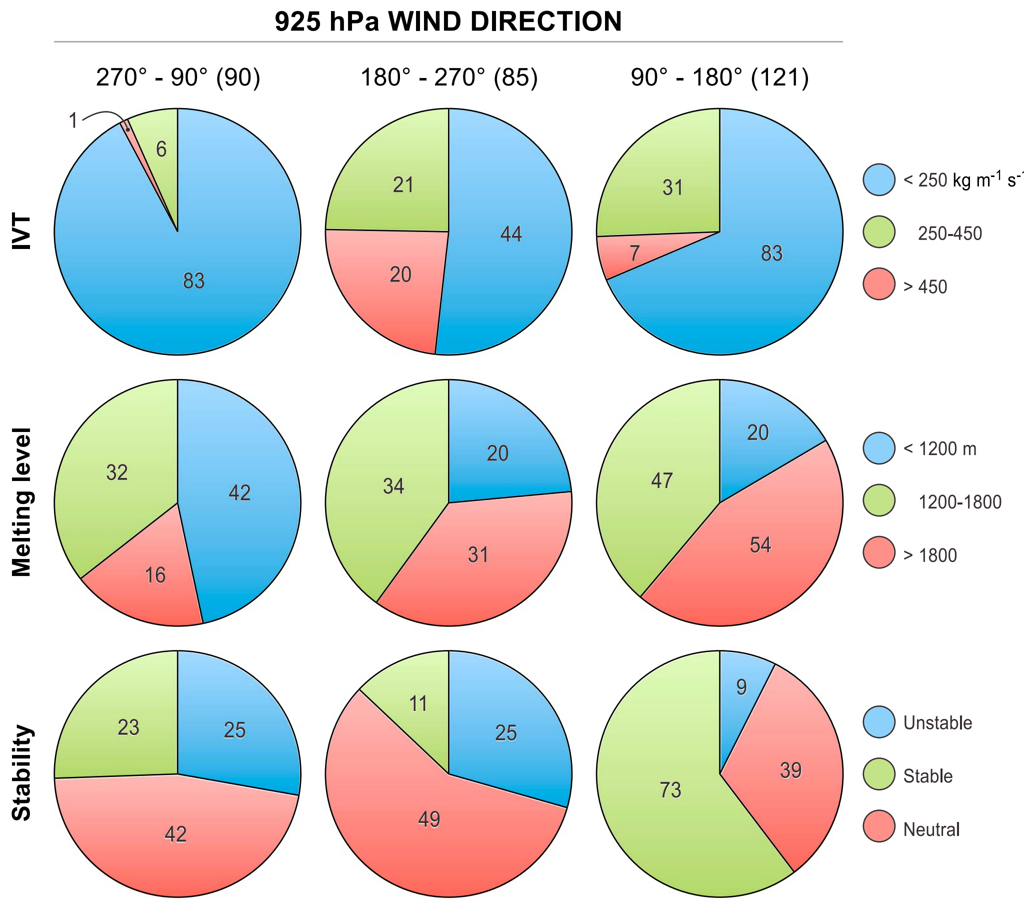

Figure 7. As in Figure 6, except for wind direction: from 270° to 90° (left column), from 180° to 270° (middle column), and from 90° to 180° (right column).

observation is not surprising since the NPOL land RHIs are favorably situated to document orographic enhancement on the southwest side of the Olympic Mountains. Winds from the southwest are usually associated with moderate to high melting level heights and neutral stability (Figure 7) but are also associated with other categories of these environmental parameters including a wide range of IVT. When the 925-hPa wind direction is from the southeast, the southeast side of the Olympic Mountains becomes the windward slope at low-levels; windward enhancement on the southeast side of the Olympic Mountains was not appropriately sampled by the NPOL radar. However, during prefrontal conditions when a storm is approaching the Olympic Peninsula, the winds tend to veer with height due to warm advection from the southeast to the southwest so that the winds at levels above 800 hPa are often from the southwest (e.g., see Figure 10 of Zagrodnik et al., 2018). These upper-level southwest winds impinge on the upper portions of the Olympic Mountains and are lifted, thus possibly providing an explanation for the weak increase in reflectivity over the land sector above 4 km seen in Figure 5f for southeast winds. Low-level southeast winds on the coast to the west of the Olympic Mountains were commonly associated with stable conditions during OLYMPEX (Figure 7). Past studies have shown that coastal southeast winds can occur commonly when low-level flow is blocked by the terrain and the onshore flow associated with an approaching synoptic storm is lifted over this blocked layer, thus providing a mechanism for enhancement on the forward slopes of the higher terrain and even further west over the ocean in the near-shore waters (Colle & Mass, 1996; James & Houze, 2005; Medina et al., 2007). This mechanism potentially reduces the differences in reflectivity between the ocean and land sectors. In contrast, when there is deep southeasterly flow such that the wind direction is from the southeast at the 700-hPa level, the difference between the land and ocean CFAD is opposite of the other environmental scenarios with a higher occurrence of higher reflectivity values

10.1029/2018JD029161

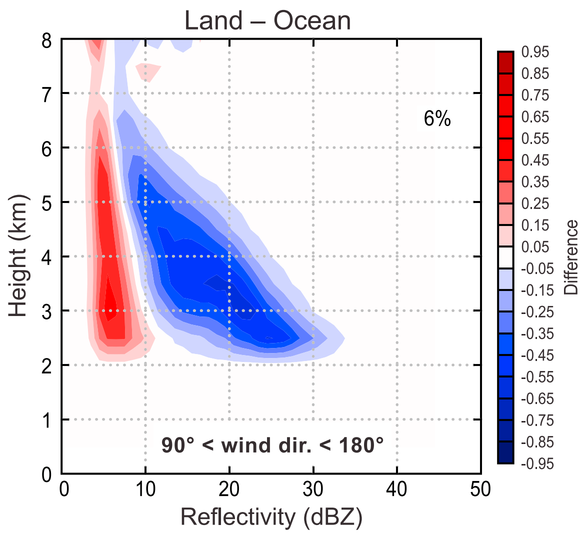

Figure 8. As in Figure 5 except for wind direction at the 700-hPa level.

over the ocean compared to over land (Figure 8). Evidently maintenance of dry continental air at middle to upper levels and downslope flow at lower levels act to suppress precipitation processes on the west side of the Olympic Mountains. This scenario is relatively rare; it occurred only 6% of the time during the period of study.

Similar to other environmental parameters, there is variability in differences between the land CFADs and the ocean CFADs for the different categories of melting level (Figures 5g–5i, third row). When the melting level is above 1,800 m, the differences are large at all levels and especially strong between 2–3 km (around the height of the melting level for warm events) and 4–5 km (~1.5–3 km above the melting level). When the melting level is between 1,200 and 1,800 m, the differences between land and ocean CFADs are moderate and only evident above 3 km (the melting level is below the 2-km minimum height threshold in these CFADs). When the melting level is below 1,200 m, the differences between the land and ocean CFADS are weak and nearly absent. Low melting level heights are most commonly associated with low IVT, northerly component winds, from 270° to 90°, and moist unstable conditions (Figure 9). These conditions are typical of unstable postfrontal periods, which are more convective in nature. The lack of difference between the ocean and land may be partially due to sampling issues as not all of the convective cells over the ocean observed by the wide NPOL west-facing RHI sector moved into the narrower RHI sector over the windward slopes (see examples in section 5). As with IVT, different thresholds of melting level height

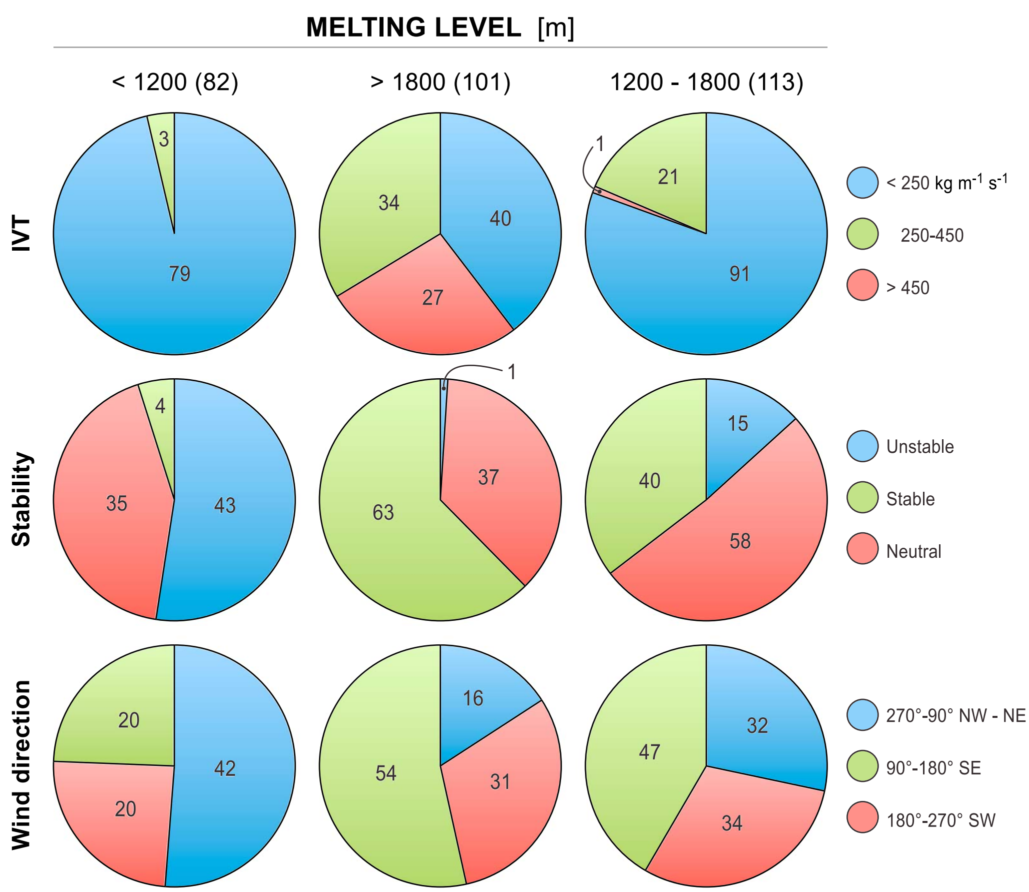

Figure 9. As in Figure 6 except for melting level height: less than 1,200 m (left column), greater than 1,800 m (middle column), and between 1,200 and 1,800 m (right column).

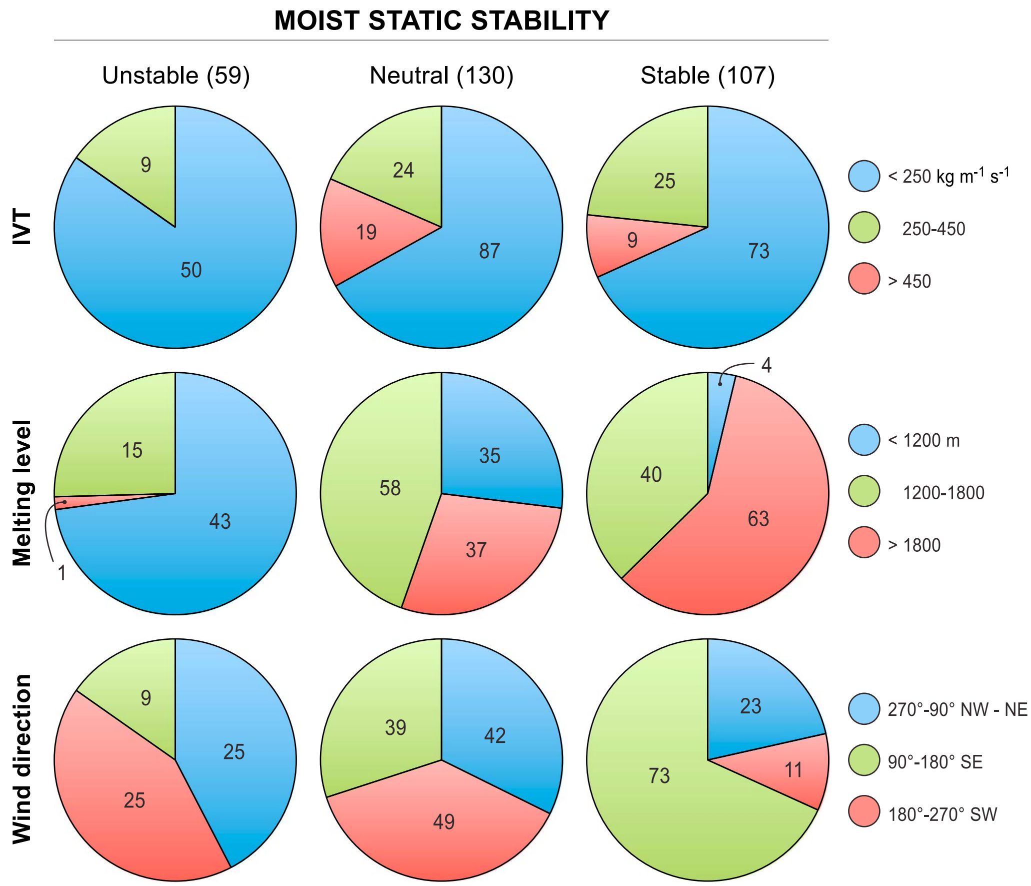

Figure 10. As in Figure 6 except for moist static stability: unstable (left column), neutral (middle column), and stable (right column). See text for precise definitions of each stability category.

±200 m (e.g., melting level <1.0 km or melting level <1.4 km) were tested and the conclusions remained unchanged.

All stability conditions exhibit higher frequency of occurrence of larger reflectivity values aloft over the land with the enhancement most pronounced during neutral stability (Figures 5j–5l, fourth row). Neutral conditions can occur under all categories of the other environmental parameters (Figure 10), with a slight preference for southwesterly winds and high IVT.

5. Examples of NPOL RHIs for Different Environmental Conditions

In the previous section, the largest differences between the land and ocean CFADs occurred during periods of high IVT (greater than 450 kg m^{-1} s^{-1}), southwest winds, high melting level (greater than 1,800 m), and neutral conditions (Figure 5). A representative example when all these conditions were met is shown in Figure 11, where ocean (left, azimuth angle 224°) and land (right, azimuth angle 54°) NPOL RHIs are displayed from 0200 and 0212 UTC, respectively, on 13 November 2015. At this time, NPOL was sampling the warm sector of a broad, long-lived, frontal system with IVT of 466 kg m^{-1} s^{-1}, melting level height 2,244 m, southwesterly 925-hPa wind direction, and neutral stability as determined by NARR data (see Zagrodnik et al., 2018, for a complete discussion of the storm). A pronounced brightband around 2.5-km elevation is evident in the reflectivity fields (Figures 11a and 11b) over both the ocean and land RHIs, with the reflectivity particularly strong and more continuous within the brightband over the land. A secondary reflectivity maximum aloft around the 5-km height level is clearly evident in the land RHI and absent in the ocean RHI and corresponds to the area of peak enhancement in the CFADs over terrain (Figures 4 and 5). This observation supports the suggestion of Medina et al. (2007) that the secondary maximum aloft is a result of the dynamic interaction of the

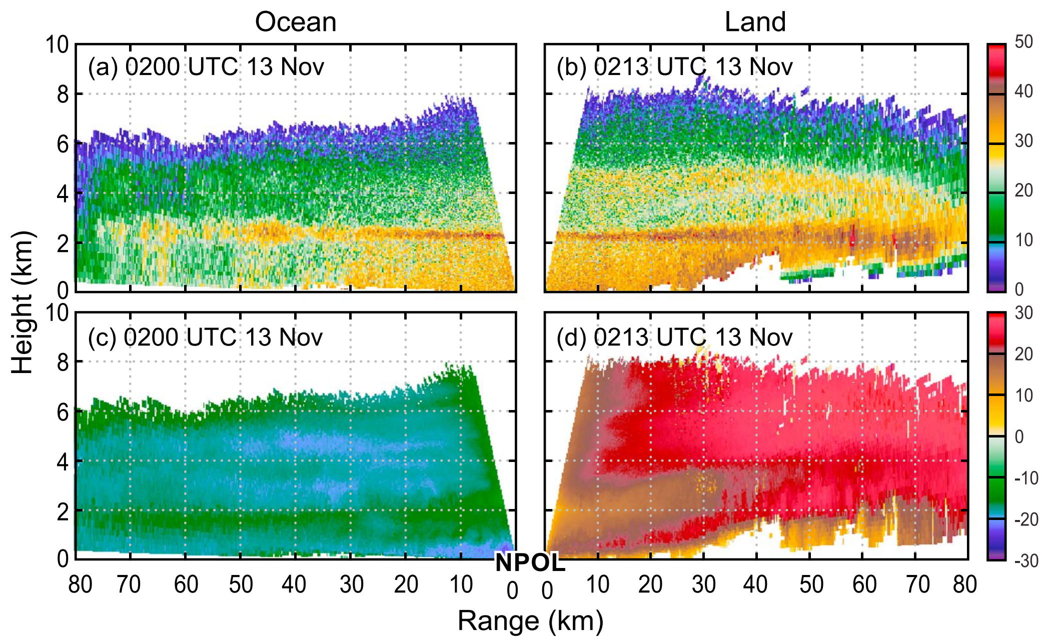

Figure 11. NPOL RHI images of (a) reflectivity at 0200 UTC 13 November at an azimuth angle of 224° (ocean), (b) reflectivity at 0213 UTC 13 November at an azimuth angle of 54° (land), (c) radial velocity at 0200 UTC 13 November at an azimuth angle of 224° (ocean), and (d) radial velocity at 0213 UTC 13 November at an azimuth angle of 54° (land). Negative values of velocity (in blues and greens) denote air moving toward the radar and positive values of velocity (in yellows and reds) denote air moving away from the radar.

baroclinic system with the terrain and not necessarily an intrinsic feature of the synoptic system as postulated by Kingsmill et al. (2006). This secondary maximum in reflectivity occurs within a region of incoming winds increasing with height as a strong low-level jet below 1 km directed toward the radar (Figure 11c) is lifted over the terrain (Figure 11d). This low-level jet lifting contributed to the production of small drops through collision and coalescence and enhanced precipitation on the windward slopes and is described in Zagrodnik et al. (2018). However, the lifting of the moist neutral air evident over a deep layer in the radial velocity field in the land RHI (Figure 11d) suggests a contribution to the initiation, growth, and aggregation of ice particles that may have led to enhancement aloft seen in the reflectivity field (Figure 11b). These microphysical details are the focus of a future paper using dual-polarization radar and in situ aircraft data from OLYMPEX.

In contrast to the large enhancement in reflectivity over land during the warm, moist, neutral events, the smallest difference between the land and ocean CFADs occurred when the melting level was below 1,200 m (Figure 5g). Low melting level was almost always associated with low values of IVT and was associated with unstable conditions and winds from the NW for more than 50% of the time (Figure 9), especially during postfrontal periods. To illustrate potential reasons why there was little contrast between the land and ocean CFADs for low melting level height, examples of ocean and land RHIs during two different postfrontal periods that met these criteria are shown in Figure 12. Postfrontal convective cells formed over water and moved onshore on both days. At NPOL on 13 December the melting level height was 878 m, IVT was 152 kg m^{-1} s^{-1}, the wind direction was from 270°, and the moist static stability was -0.47 s^{-2} 10^{-4}. During the 13 December case, the individual cells were relatively narrow over the ocean and broader horizontally over land but exhibited roughly the same echo-top height of close to 6 km and similar reflectivity values above 2 km. At NPOL on 18 December the melting level height was 998 m, IVT was 85 kg m^{-1} s^{-1}, wind direction was from 270°, and the moist static stability was -0.30 s^{-2} 10^{-4}. The 18 December example shows higher reflectivity in an individual cell about 50 km offshore from NPOL that reached 4 km in height whereas a smaller, narrower cell around 40 km from NPOL was sampled over land. There is also a thin horizontal layer of low reflectivity (around 10 dBz) at the 4-km level that is slightly deeper in extent over land. These examples demonstrate the variability found in postfrontal convective showers. Although we noted the broadening of

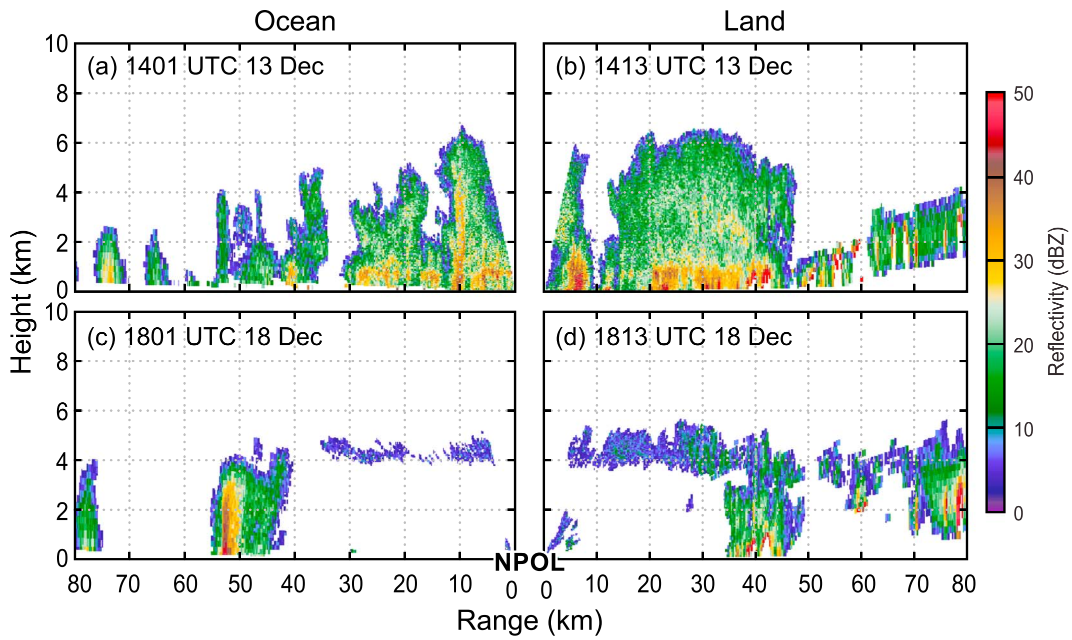

Figure 12. NPOL RHI images of reflectivity at a 1401 UTC 13 December at an azimuth angle of 230° (ocean), (b) 1413 UTC 13 December at an azimuth angle of 52° (land), (c) 1801 UTC 18 December at an azimuth angle of 233° (ocean), and (d) 1813 UTC 18 December at an azimuth angle of 52° (land).

postfrontal showers as they progressed onshore and over the windward slopes during OLYMPEX (e.g., Figure 12b), a behavior also observed in earlier studies (e.g., Medina et al., 2007), this signature was not evident in the low melting level CFAD (Figure 5g). The most likely reason for little differences between the ocean and land reflectivity structure is because there were relatively few postfrontal periods sampled during OLYMPEX. Due to the random cellularity of postfrontal showers, it would be necessary to have a large sample size to detect any significant reflectivity differences between the ocean sector and the land sector. In addition, low melting level heights also occurred during other meteorological conditions, such as during cold (most likely occluded) storm systems, or during early prefrontal conditions where warm air is approaching aloft but low-level cold air is still in residence from the prior storm system. As shown in Figure 9, these other scenarios contributing to low melting level heights were less frequent than the typical postfrontal conditions of low IVT, unstable flow from the west-northwest. Example RHIs from early prefrontal conditions with low melting level generally showed stratiform conditions with increasing cloud thickness as the storm system progressed eastward and little reflectivity differences between land and ocean (not shown).

6. Comparison to Satellite-Derived Radar Reflectivity

In order to test if the DPR is capable of reproducing the precipitation structures in regions of complex terrain described in this study, CFADs from the DPR Ku and Ka bands were calculated from all the GPM overpasses during the cold season over the Olympic Peninsula and adjacent ocean region (see section 2.4 for exact regions). The difference between the ocean and land DPR reflectivity CFADs is shown in Figure 13. Even though these regions are broader than the NPOL ocean and land RHI sectors, the same reflectivity enhancement over land in the range from 4 to 6 km and higher reflectivity in the vicinity of the bright-band at 2–3 km is evident in both difference CFADs. The reflectivities in rainy areas and at the bright band tend to be lower for DPR Ka band and the difference CFAD (Figure 13b) shows a weaker enhancement over land at those altitudes than the Ku band. These encouraging results show that GPM's DPR at both frequencies is capable of detecting the precipitation enhancement processes aloft in the ice layer over complex terrain.

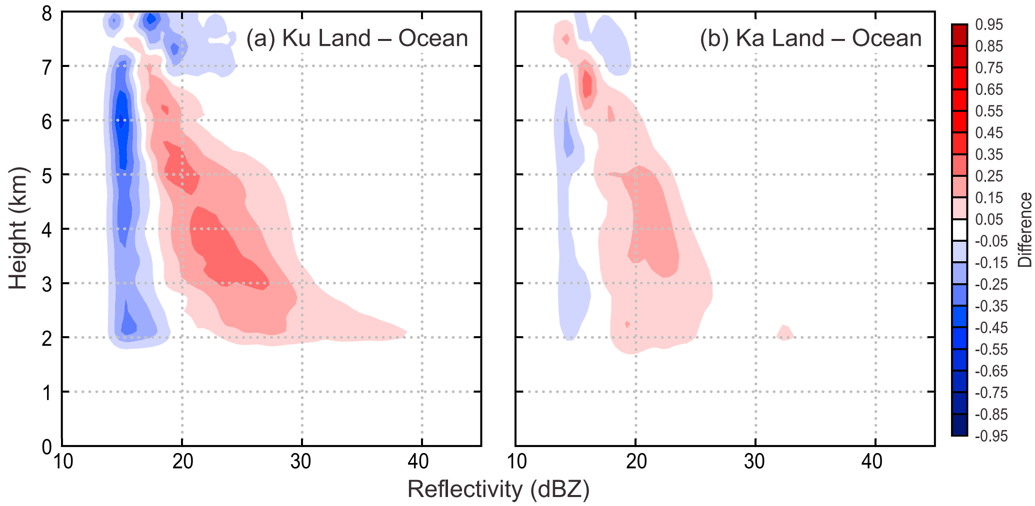

Figure 13. The difference between the normalized reflectivity CFAD from the GPM DPR Ku band (a) and Ka band (b) over the land area and over the ocean area. Red (blue) shades indicate relatively higher (lower) frequencies of reflectivity over land compared to over ocean.

7. Discussion and Conclusions

Orographic enhancement of precipitation processes aloft is documented using reflectivity data from the NPOL S-band scanning radar that was situated on the west coast of Washington State during the OLYMPEX GV field campaign from November 2015 through mid-January 2016. NPOL obtained numerous high-resolution vertical cross sections (RHIs) of reflectivity over the ocean and over land. These RHI data were compared using CFADs. Differences between the land and ocean CFADs highlight a higher frequency of occurrence of larger reflectivities for all heights between 2 and 8 km over land compared to ocean with the largest difference in the 4- to 6-km height range, indicating a robust signature of orographic enhancement aloft over the complex terrain (Figure 4). This study is the first of which we are aware that provides statistical analysis of research quality RHIs observed upwind where the flow is less affected by mountains and observed downwind over the windward slopes. Although this analysis was performed over the Olympic Mountains during the OLYMPEX experiment, these results are applicable to all coastal mountain ranges located downwind of oceanic midlatitude baroclinic storm tracks. West coastal mountain ranges intercept frontal systems in South America, New Zealand, northern California, and northwestern North America.

This pattern of enhancement aloft is seen to some degree under all environmental conditions considered in this study but is particularly pronounced during periods of high IVT (greater than 450 kg m^{-1} s^{-1}), high melting level (greater than 1,800 m), southwest low-level winds, and neutral stability (Figures 5b, 5e, 5h, and 5k); conditions generally associated with the warm sector portions of midlatitude cyclones and atmospheric river conditions such as those described in Neiman et al. (2002), Ralph et al. (2004), and Zagrodnik et al. (2018). Our results corroborate those found by Medina et al. (2007), who found a secondary enhancement in reflectivity 1–2.5 km above the brightband during the middle sector period (i.e., the warm sector) of storms passing over the Oregon Cascade Mountains. Even if this secondary enhancement aloft were an intrinsic part of the synoptic scale system as postulated by Kingsmill et al. (2006), our results clearly show that there is further significant enhancement as deep moist-neutral, high water vapor content flow is lifted when it encounters the mountain range.

The differences between the land and ocean CFADs were smallest during periods of low melting level height most commonly associated with postfrontal conditions and usually accompanied by low IVT, moist unstable, and low-level winds from the northwest (Figure 5g). The lack of significant enhancement aloft seen during these periods is partially due to the small sample of such cases in OLYMPEX, the shallow, small-scale, and random nature of the convective elements, and the difference in sector size between the ocean and the land RHIs. The only environmental condition that did not show an enhancement over land was during deep easterly flow (Figure 8) when there was no onshore flow over the terrain.

This orographic enhancement pattern is also evident in differences between CFADs produced from reflectivity measured by GPM DPR over a box encompassing the Olympic Peninsula and a box to the immediate west over the ocean. This result has implications for satellite retrievals of rain and snow based on satellite-based reflectivity measurements. In general, reflectivity cannot be retrieved from the DPR in the lowest 1–2 km due to ground clutter (Skofronick-Jackson et al., 2017). Zagrodnik et al. (2018) showed that precipitation processes of collision and coalescence below the melting level (generally below 2–3 km) during warm precipitation events was an important contributor to the overall rain rates observed on the windward slopes of the Olympic Mountains, thus casting some doubt on GPMs potential to accurately detect the enhancement of precipitation in complex terrain. However, we demonstrate here that GPM was able to detect the reflectivity increase aloft over terrain thus showing a potential for GPM to provide good estimates of precipitation structure and distribution over remote mountainous regions.

Additional questions remain, however, about the specific particles associated with this upper-level reflectivity enhancement over terrain and the processes that create the particles. Past studies have demonstrated that flow can be lifted over blocked or stable layers ahead of a mountain barrier. The resulting turbulent overturning along shear layers can enhance growth of particles by riming and aggregation (Houze & Medina, 2005; Medina & Houze, 2003, 2015; Rotunno & Houze, 2007). During periods of near neutral conditions and high IVT, the flow is more easily lifted and processes of collision and coalescence below the melting level and riming and aggregation above the melting level provide mechanisms for enhanced particle growth (Medina et al., 2007; Medina & Houze, 2003; Rotunno & Houze, 2007; Zagrodnik et al., 2018). Through a more detailed study of the ground-based radar data, including periods with coincident in situ aircraft probe data and airborne radar data transecting the high terrain, the dynamical, and microphysical processes leading to the reflectivity enhancement documented here, and whether the observed processes are similar to those found in past studies will be explored. This topic is a focus for follow-on studies.

Acknowledgments

The authors thank the Quinault Indian Nation for permission to install the NPOL radar on their land and the scientists and NASA engineers who were operating NPOL during all hours and under all conditions during OLYMPEX. Beth Tully provided graphics support. This research was supported by NASA grants NNX16AK05G, NNX16AD75G, and 80NSSC17K0279 and NSF grants AGS-1503155 and AGS-1657251. All OLYMPEX data used in this investigation are found on the NASA OLYMPEX data archive https://doi.org/10.5067/GPMGV/OLYMPEX/DATA101 and are referenced below in Petersen et al. (2018), Rutledge et al. (2018), and Wolff et al. (2017). The NARR data are referenced below and were obtained from https://www.esrl.noaa.gov/psd/data/gridded/data.narr.html. The DPR data were obtained from Iguchi and Meneghini (2016a, 2016b), and the regridded DPR data as described in the text are available at gpm.atmos.washington.edu.

References

Ciesielski, P. E., Haertel, P. T., Johnson, R. H., Wang, J., & Loehrer, S. (2012). Developing high-quality field program sounding datasets. *Bulletin of the American Meteorological Society*, *93*(3), 325–336. https://doi.org/10.1175/BAMS-D-11-00091.1

Colle, B. A., & Mass, C. F. (1996). An observational and modeling study of the interaction of low-level southwesterly flow with the Olympic Mountains during COAST IOP 4. *Monthly Weather Review*, *124*(10), 2152–2175. https://doi.org/10.1175/1520-0493(1996)124<2152:AOAMSO>2.0.CO;2

Daly, C., Neilson, R., & Phillips, D. (1994). A statistical topographic model for mapping climatological precipitation over mountainous terrain. *Journal of Applied Meteorology*, *33*, 140–158. https://doi.org/10.1175/1520-0450(1994)033<0140:ASTMFM>2.0.CO;2

Durran, D. R., & Klemp, J. B. (1982). On the effects of moisture on the Brunt-Väisälä frequency. *Journal of Atmospheric Science*, *39*(10), 2152–2158. https://doi.org/10.1175/1520-0469(1982)039<2152:OTEOMO>2.0.CO;2

Garvert, M. F., Smull, B., & Mass, C. (2007). Multiscale mountain waves influencing a major orographic precipitation event. *Journal of Atmospheric Science*, *64*(3), 711–737. https://doi.org/10.1175/JAS3876.1

Houze, R. A. Jr., James, C. N., & Medina, S. (2001). Radar observations of precipitation and airflow on the Mediterranean side of the Alps: Autumn 1998 and 1999. *Quarterly Journal of the Royal Meteorological Society*, *127*(578), 2537–2558. https://doi.org/10.1002/qj.49712757804.

Houze, R. A. Jr., McMurdie, L. A., Petersen, W. A., Schwaller, M. R., Baccus, W., Lundquist, J., et al. (2017). The Olympic Mountains Experiment (OLYMPEX). *Bulletin of the American Meteorological Society*, *98*(10), 2167–2188. https://doi.org/10.1175/BAMS-D-16-0182.1

Houze, R. A. Jr., & Medina, S. (2005). Turbulence as a mechanism for orographic precipitation enhancement. *Journal of Atmospheric Science*, *62*(10), 3599–3623. https://doi.org/10.1175/JAS3555.1

Houze, R. A. Jr., Rasmussen, K. L., Zuluaga, M. D., & Brodzik, S. R. (2015). The variable nature of convection in the tropics and subtropics: A legacy of 16 years of the Tropical Rainfall Measuring Mission satellite. *Reviews of Geophysics*, *53*, 994–1021. https://doi.org/10.1002/2015RG000488

Houze, R. A., Jr., Wilton, D. C., & Smull, F. (2007). Monsoon convection in the Himalayan region as seen by the TRMM Precipitation Radar. *Quarterly Journal of the Royal Meteorological Society*, *133*, 1389–1411. https://doi.org/10.1002/qj.106

Iguchi, T., & Meneghini, R. (2016a). GPM DPR Ka precipitation profile 2A 1.5 hours 5 km V05, Greenbelt, MD, Goddard Earth Sciences Data and Information Services Center (GES DISC), Accessed: 19 September 2018.

Iguchi, T., & Meneghini, R. (2016b). GPM DPR Ku Precipitation Profile 2A 1.5 hours 5 km V05, Greenbelt, MD, Goddard Earth Sciences Data and Information Services Center (GES DISC), Accessed: 1 October 2017.

James, C. N., & Houze, R. A. Jr. (2005). Modification of precipitation by coastal orography in storms crossing northern California. *Monthly Weather Review*, *133*(11), 3110–3131. https://doi.org/10.1175/MWR3019.1

Kingsmill, D. E., Neiman, P. J., Ralph, F. M., & White, A. B. (2006). Synoptic and topographic variability of northern California precipitation characteristics in landfalling winter storms observed during CALJET. *Monthly Weather Review*, *134*(8), 2072–2094. https://doi.org/10.1175/MWR3166.1

Lewis, W. R., Steenburgh, W. J., Alcott, T. I., & Rutz, J. (2017). GEFS precipitation forecasts and the implications of statistical downscaling over the western United States. *Weather and Forecasting*, *32*(3), 1007–1028. https://doi.org/10.1175/WAF-D-16-0179.1

Medina, S., & Houze, R. A. Jr. (2003). Air motions and precipitation growth in Alpine storms. *Quarterly Journal of the Royal Meteorological Society*, *129*(588), 345–371. https://doi.org/10.1256/qj.02.13

Medina, S., & Houze, R. A. Jr. (2015). Small-scale precipitation elements in midlatitude cyclones crossing the California Sierra Nevada. *Monthly Weather Review*, *143*(7), 2842–2870. https://doi.org/10.1175/MWR-D-14-00124.1

Medina, S., Sukovich, E., & Houze, R. A. Jr. (2007). Vertical structures of precipitation in cyclones crossing the Oregon Cascades. *Monthly Weather Review*, *135*(10), 3565–3586. https://doi.org/10.1175/MWR3470.1

Mesinger, F., DiMego, G., Kalnay, E., Mitchell, K., Shafran, P. C., Ebisuzaki, W., et al. (2006). North American Regional Reanalysis. *Bulletin of the American Meteorological Society*, *87*(3), 343–360. https://doi.org/10.1175/BAMS-87-3-343

Minder, J. R., Durran, D. R., Roe, G. H., & Anders, A. M. (2008). The climatology of small-scale orographic precipitation over the Olympic Mountains: Patterns and processes. *Quarterly Journal of the Royal Meteorological Society*, *134*(633), 817–839. https://doi.org/10.1002/qj.258

Moore, B. J., Neiman, P. J., Ralph, F. M., & Barthold, F. (2012). Physical processes associated with heavy flooding rainfall in Nashville, Tennessee and vicinity during 1–2 May 2012: The role of an atmospheric river and mesoscale convective systems. *Monthly Weather Review*, *140*(2), 358–378. https://doi.org/10.1175/MWR-D-11-00126.1

Nagle, R. E., & Serebreny, S. M. (1962). Radar precipitation echo and satellite cloud observations of a maritime cyclone. *Journal of Applied Meteorology*, *1*, 279–295. https://doi.org/10.1175/1520-0450(1962)001<0279:RPEASC>2.0.CO;2

Neiman, P. J., Hughes, M., Moore, B. J., Ralph, F. M., & Sukovich, E. M. (2013). Sierra barrier jets, atmospheric rivers, and precipitation characteristics in northern California: A composite perspective based on a network of wind profilers. *Monthly Weather Review*, *141*(12), 4211–4233. https://doi.org/10.1175/MWR-D-13-00112.1

Neiman, P. J., Ralph, F. M., White, A. B., Kingsmill, D. E., & Persson, O. G. (2002). The statistical relationship between upslope flow and rainfall in California's coastal mountains: Observations during CALJET. *Monthly Weather Review*, *130*(6), 1468–1492. https://doi.org/10.1175/1520-0493(2002)130<1468:TSRBUF>2.0.CO;2

Neiman, P. J., Schick, L. J., Ralph, F. M., Hughes, M., & Wick, G. A. (2011). Flooding in western Washington: The connection to atmospheric rivers. *Journal of Hydrometeorology*, *12*(12), 1337–1358. https://doi.org/10.1175/2011JHM1358.1.2011

NOAA/OAR/ESRL PSD (2004). North American Regional Reanalysis Data from NCEP Global Reanalysis, accessed 24 August 2016. Retrieved from https://www.esrl.noaa.gov/psd/data/gridded/data.narr.html

Nuss, W. A., & Miller, D. F. (2001). Mesoscale predictability under various synoptic regimes. *Nonlinear Processes in Geophysics*, *8*, 429–438. https://doi.org/10.5194/npg-8-429-2001

Petersen W., Houze, R. A. Jr., & McMurdie, L. A. (2018). GPM Ground Validation OLYMPEX Field Campaign Data Collection. Data set available online http://ghrc.nsstc.nasa.gov/ from the NASA EOSDIS Global Hydrology Resource Center Distributed Active Archive Center Huntsville, Alabama, U.S.A. accessed 16 September 2016. https://doi.org/10.5067/GPMGV/OLYMPEX/DATA 101

Picard, L., & Mass, C. (2017). Sensitivity of orographic precipitation to flow direction: An idealized modeling approach. *Journal of Hydrometeorology*, *18*(6), 1673–1688. https://doi.org/10.1175/JHM-D-16-0209.1

Pippitt, J. L., Wolff, D. B., Petersen, W. A., & Marks, D. A. (2015). Data and operational processing for NASA's GPM ground validation Program Presentation at the 37th Conference on Radar Meteorology, Norman, OK, 14–18 September, 2015. Retrieved from https://ams.confex.com/ams/37RADAR/webprogram/Paper275627.html

Purnell, D. J., & Kirshbaum, D. J. (2018). Synoptic control over orographic precipitation distributions during the Olympic Mountains Experiment (OLYMPEX). *Monthly Weather Review*, *146*(4), 1023–1044. https://doi.org/10.1175/MWR-D-17-0267.1

Ralph, F. M., Neiman, P. J., & Wick, G. A. (2004). Satellite and CALJET aircraft observations of atmospheric rivers over the eastern North Pacific Ocean during the winter of 1997/98. *Monthly Weather Review*, *132*(7), 1721–1745. https://doi.org/10.1175/1520-0493(2004)132<1721:SACAOO>2.0.CO;2

Rotunno, R., & Houze, R. A. Jr. (2007). Lessons on orographic precipitation from the Mesoscale Alpine Programme. *Quarterly Journal of the Royal Meteorological Society*, *133*, 811–830. https://doi.org/10.1002/qj.67

Rutledge, S. A., Young, K., Voemel, H., Hudak, D, & Rodriguez, P. (2018). GPM Ground Validation Upper Air Radiosonde OLYMPEX. Dataset available online from the NASA Global Hydrology Center DAAC, Huntsville, Alabama, U.S.A. https://doi.org/10.5067/GPMGV/OLYMPEX/RADIOSONDES/DATA 101

Rutz, J. J., Steenburgh, W. J., & Ralph, F. M. (2014). Climatological characteristics of atmospheric rivers and their penetration over the western United States. *Monthly Weather Review*, *142*(2), 905–921. https://doi.org/10.1175/MWR-D-13-00168.1

Skofronick-Jackson, G., Petersen, W. A., Berg, W., Kidd, C., Stocker, E., Kirschbaum, D. B., et al. (2017). The Global Precipitation Measurement (GPM) Mission for Science and Society. *Bulletin of the American Meteorological Society*, *98*(8), 1679–1695. https://doi.org/10.1175/BAMS-D-15-00306.1

Smith, R. B., & Barstad, I. (2004). A linear theory of orographic precipitation. *Journal of the Atmospheric Sciences*, *61*(6), 1377–1391. https://doi.org/10.1175/1520-0469(2004)061<1377:ALTOOP>2.0.CO;2

Steenburgh, W. J. (2003). One hundred inches in one hundred hours: Evolution of a Wasatch Mountain winter storm cycle. *Weather and Forecasting*, *18*(12), 1018–1036. https://doi.org/10.1175/1520-0434(2003)018<1018:OHIIOH>2.0.CO;2

Toyoshima, K., Masunaga, H., & Furuzawa, F. A. (2015). Early evaluation of Ku- and Ka-band sensitivities for the Global Precipitation Measurement (GPM) Dual-Frequency Precipitation Radar (DPR). *SOLA*, *11*, 14–17. https://doi.org/10.2151/sola.2015-004

Wolff, D. B., Marks, D. A., & Petersen, W. A. (2015). General application of the relative calibration adjustment (RCA) technique for monitoring and correcting radar reflectivity calibration. *Journal of Atmospheric and Oceanic Technology*, *32*, 496–506. https://doi.org/10.1175/JTECH-D-13-00185

Wolff, D. B., Marks, D. A., Petersen, W. A., & Pippit, J. (2017). GPM Ground Valdation NASA S-Das BandBand Dual Polarimetric (NPOL) Doppler Radar OLYMPEX. Dataset available online from the NASA Global Hydrology Center DAAC, Huntsville, Alabama, U. S. A. https://doi.org/10.5067/GPMGV/OLYMPEX/NPOL/DATA 301

Yuter, S. E., & Houze, R. A. Jr. (1995). Three-dimensional kinematic and microphysical evolution of Florida cumulonimbus. Part II: Frequency distributions of vertical velocity, reflectivity, and differential reflectivity. *Monthly Weather Review*, *123*(7), 1941–1963. https://doi.org/10.1175/1520-0493(1995)123<1941:TDKAME>2.0.CO;2

Zagrodnik, J. P., McMurdie, L. A., & Houze, R. A. Jr. (2018). Stratiform precipitation processes in cyclones passing over a coastal mountain range. *Journal of the Atmospheric Sciences*, *75*(3), 983–1004. https://doi.org/10.1175/JAS-D-17-0168.1